Journal of Materials Chemistry A

Accepted Manuscript

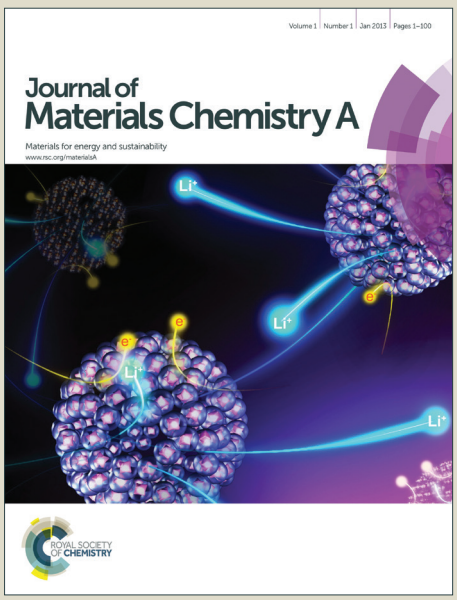

ROYAL SOCIETY OF CHEMISTRY

www.rsc.org/materialsA

Journal Name

RSCPublishing

ARTICLE

Evolution of nanoscale morphology in single and binary metal oxide microparticles during reduction and oxidation processes

Cite this: DOI: 10.1039/xoxxoooooox

Received ooth January 2012,
Accepted ooth January 2012

DOI: 10.1039/xoxxoooooox

www.rsc.org/

Lang Qin,[a] Ankita Majumder,[a] Jonathan A. Fan,[b] David Kopechek,[a] and Liang-Shih Fan[a]*

Metal oxide composites are enabling materials for many energy conversion systems such as chemical looping and photocatalysis. Their synthesis into electronic materials and operation in chemical looping technologies are based on reduction and oxidation reactions that involve exchanges of ions and electrons. These processes result in the creation and diffusion of defects that determine the nanoscale crystal phases and morphologies within these materials and their subsequent bulk chemical and electrical behavior. In this study, samples of metal oxide composites undergoing cycles of reduction and oxidation are examined at the nano- and micro–scale; the interfacial characteristics of dissimilar metals and metal oxides within the composites are examined. Specifically, structural transformations during redox processes involving pure Fe, FeNi alloy, and CuNi alloy microparticles are investigated. In Fe and FeNi systems, nanowires and nanopores are observed to simultaneously form on the microparticle surface during oxidation, while no such structuring is observed in the CuNi system. Additionally, uniform FeNi microparticles are transformed into particles with a NiO-rich core and Fe_2O_3-rich shell during oxidation, due to differences in the oxidation and ion diffusion rates of Ni and Fe. In all material systems, the oxidized form of the microparticles exhibited porous cores due to ion transport described by the Kirkendall effect. A fundamental understanding of these phenomena will help direct the fabrication of electronic oxide materials and the development of metal oxide-based oxygen carriers for chemical looping applications.

1. Introduction

Metal oxides are among the most versatile materials in the energy industry and can exhibit a wide range of physical and chemical properties. In particular, composites of metal oxides are enabling materials for operation in many energy conversion systems, including solar panels,[1] fuel cells,[2] photocatalysis,[3] and chemical looping systems.[4] The electrical, optical, and chemical properties of metal oxides and their composites are determined by their crystal phases and morphologies. Consequently, it is critical to understand the diffusion of defects and to control the morphology of these materials during processes associated with material growth, such as the high temperature oxidation of metals to form metal oxides, and their associated reduction reactions. Metal oxides, their composites, and the reduction and oxidation reactions conducted in this study are of special relevance to chemical looping systems.

For many of these applications, oxide material performance can be enhanced by their nanoscale processing. For semiconducting oxides with electronic and optoelectronic functionality, such as Fe_2O_3 in photocatalysis, the position of electron energy bands and the magnitude of electronic transition energies within these nanomaterials directly correlate with the crystal phase and the material geometry itself, due to quantum confinement effects. Additionally, the electronic performance of these materials can be enhanced when the nanostructure length scale is comparable to or smaller than the electron and hole diffusion length scales.[5] Oxide nanostructuring also enables the photonic properties of the materials, such as frequency-selective light trapping and absorption, to be engineered. For all of these applications, it is imperative to understand how to control the precise metal oxide morphology during oxidative growth.

The nanoscale morphology of metal oxides also plays a significant role in chemical looping, which is regarded as a promising technique in the U.S. Department of Energy's roadmap[6,7] toward cost effective technology solutions for CO_2

capture from carbonaceous fuels.[8] A chemical looping system converts carbonaceous fuels to energy using metal oxide based oxygen carriers and can operate under various modes.[9] In the chemical looping gasification (CLG) mode, hydrogen and heat are co-generated,[6] while the oxygen carriers circulate among three reactors: a reducer, an oxidizer, and a combustor. In the chemical looping combustion (CLC) mode, the oxidizer is excluded and the oxygen carriers are completely oxidized only in the combustor, thus producing only heat. The chemical looping oxygen uncoupling (CLOU) process mode is based on CLC and uses metal oxides to release gaseous oxygen to convert solid fuels. In all of these modes of chemical looping operation, the diffusion of metal ions, oxygen ions, and oxygen vacancies dictates redox reactivity and recyclability of the metal oxide oxygen carriers.[10]

Transition metal oxides, including Fe, Ni, Mn, Cu, and Co, as well as alkaline earth metals such as Ca have been extensively studied as active oxygen carrier materials in CLC, CLG, and CLOU.[11,12,13,14] While single metal oxide systems can display high levels of reactivity, combinations of binary active metal oxide systems, such as nickel-iron oxide and copper-nickel oxide, have shown even better reactivity for certain reactions.[15,16] For example, it has been demonstrated that while CuO allows for full conversion of methane to CO_2 and H_2O, the addition of NiO to the CuO system helps stabilize the low-melting CuO phase during CLC.[17] Similarly, it was found that mixed NiO and Fe_2O_3[18] carriers have increasing reactivity with increasing Ni content. However, the mechanism of oxygen transfer during these reactions is still not completely understood.

In this work, we examine active single and binary metallic microparticle systems undergoing cycles of redox reactions, and we investigate the phenomena associated with nanoscale ion diffusion. The microparticles have diameters of 10-30μm and are single crystalline,[10] which eliminates complex dynamics such as ionic diffusion at grain boundaries during the initial oxidation cycle. We study particles with three different compositions: pure Fe metal, FeNi alloy, and CuNi alloy. The effects induced by ion and defect diffusion occurring deep within the microparticle cores are investigated by using focused ion beam nanomachining to visualize the composition and morphology of individual microparticle cross-sections. The formation of nanostructures on the surfaces of the three systems is attributed to a stress-driven self-organization process[19] and we discuss mechanisms associated with the morphological and phase transformations that arise from the redox reactions. The systems studied do not include inert metal oxide supports so that we can focus on the intrinsic characteristics of the redox reactions of the active metals alone. We note that particles optimized for recyclability in chemical looping processes require an inert oxide support, such as Al_2O_3 or TiO_2, which alters the diffusion mechanism of ions within the composite particle.

2. Experimental

Fe, FeNi and NiCu powders (99%+ purity) with 325 mesh were purchased from Alfa Aesar. An SEM analysis shows particle sizes between 10 and 60μm. The powders were washed with acetone three times and dried at room temperature prior to further examination. Approximately 0.1g powder samples were mounted in an alumina crucible and run through either one oxidation step or between one and five oxidation-reduction cycles at 700°C using a Setaram SETSYS Evolution Thermogravimetric Analyzer (TGA). Oxidation was performed using a 200 mL/min flow of gas consisting of 50% air balanced with N_2. The reduction step used a 200 mL/min flow of gas containing 50% H_2 balanced with N_2. The oxidation and reduction steps lasted for 30 minutes each and were alternated with an intermediate 10 minute flushing step using N_2 at 100 ml/min. All samples were analyzed using a Rigaku SmartLab X-Ray Diffractometer (XRD) with eliminated fluorescence. Scans were run from 30-80 degrees at a rate of 1 degree per minute with an accelerating voltage and filament current of 40kV and 44mA, respectively. All the XRD spectra were analyzed using PDXL software and identified with the JCPDF database. Phase identification and corresponding JCPDF No. are listed in Table 1.

Table 1. Identified sample phases from XRD

Sample	Cycle number	Crystal phase	JCPDF No.
FeNi	0	$Fe_{0.64}Ni_{0.36}$	47-1405
	0.5	Fe_2O_3	39-1346
		Fe_3O_4	75-0033
	1	$Fe_{0.64}Ni_{0.36}$	47-1405
	5	$Fe_{0.64}Ni_{0.36}$	47-1405
Fe	0	Fe	87-0721
	0.5	Fe_2O_3	39-1346
	1	Fe	87-0721
		Fe_3O_4	75-0033
	5	Fe	87-0721
		Fe_3O_4	75-0033
NiCu	0	Cu	85-1326
		Ni	70-1849
	0.5	CuO	80-1916
		NiO	78-0429
	1	Cu	85-1326
		Ni	70-1849
	5	Cu	85-1326
		Ni	70-1849
		NiO	78-0429

Scanning Electron Microscopy (SEM) samples were examined with a 20kV and 43pA electron beam. Secondary electron images were obtained with a working distance of 4.1mm. Energy dispersive X-ray spectra and 2-D material mapping were obtained using Oxford Energy Dispersive X-Ray Spectrometry (EDS) at an accelerating voltage of 20kV. Particle cross-sections

were prepared using the FEI Helios NanoLab600 DualBeam system, where samples were tilted at 52° and adjusted at the eucentric height for dual beam imaging. Ga ions were generated at an accelerating voltage of 30kV. A regular cross section was first performed at an ion beam of 2.8nA, followed by a cleaning cross section milling at 0.28nA.

3. Results and discussion

3.1. Cyclic iron redox reactions

The dramatic changes in internal morphology of the particles before and after oxidation reactions are characterized with focused ion beam nanomachining and electron microscopy to visualize cross-sections of the particles with nanoscale resolution. A cross sectional image of a typical Fe particle is shown in Figure 1(a). The original Fe particle prior to oxidation has a low density with randomly distributed pores throughout the whole particle and no visible grain boundaries. An XRD spectrum of a sample of the Fe powder (Figure 2(a)) shows that the Fe particles are in their pure phase. Particles that have undergone oxidation, on the other hand, experience substantial changes. Here, oxidation results in a mean volume expansion of approximately 25% and the formation of a porous microparticle center, as visualized in Figure 1(b). It is noted from Figure 1(b) that the porosity distribution is not as random as in Figure 1(a)

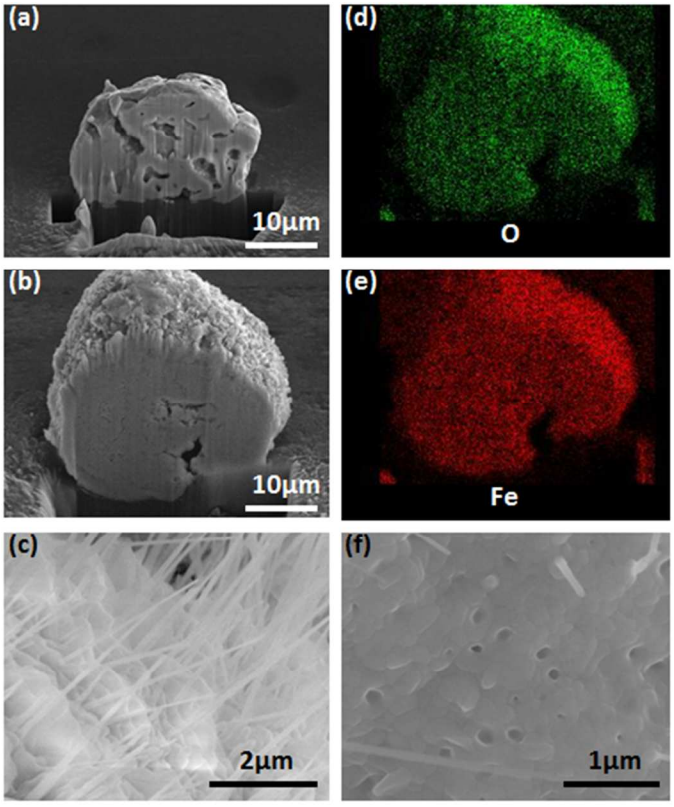

Figure 1. Characterization of Fe particle. (a) SEM image of cross-section of fresh Fe particle; (b) SEM image of cross-section of Fe_2O_3 particle after Fe oxidation; (c) and (f) SEM image of top surface of Fe_2O_3 particle; (d) EDS mapping of O from (b); (e) EDS mapping of Fe from (b)

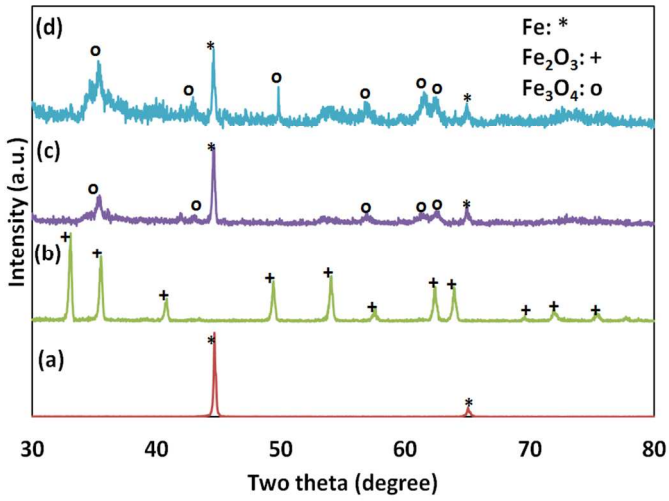

Figure 2. XRD of Fe particle. (a) fresh (b) after oxidation (c) after one oxidation-reduction cycle (d) after five oxidation-reduction cycles

and the pores are concentrated in the center of the particle. These voids in the center reflect that Fe atoms initially in the core underwent outward diffusion. This phenomenon can be ascribed to the Kirkendall effect,[20,21] which relates solid-state diffusion to an atomic concentration gradient. In this case, oxidation of Fe atoms on the surface creates a concentration gradient which causes Fe atoms to continuously diffuse from the core to the surface, leading to the formation of the porous center. Fe atoms are ionized during the diffusion process and ionic diffusion occurs through vacancy exchange, as opposed to the direct interchange of atoms. Here, Fe oxidation can be regarded as consumption of oxygen vacancies $V_{\ddot{O}}$:

$$\tfrac{1}{2}O_2 + V_{\ddot{O}} = O_O^X + 2h \qquad (1)$$

To summarize, oxygen ions diffuse inward to fill in $V_{\ddot{O}}$ and Fe ions diffuse outward to react with oxygen ions. The formation of the porous microparticle center arising from these diffusion events can be explained by the following. First, the outward Fe diffusion coefficient ($9.7x10^{-15}cm^2/s$)[22] is higher than the inward oxygen diffusion coefficient ($5.2x10^{-16}cm^2/s$) in Fe_2O_3 at 700°C, which results in net Fe transport from the center of the microparticle to the particle edge.[23] This outward Fe transport is further enhanced because the 25% volume expansion rate of Fe to Fe_2O_3 creates physical space for the Fe ions to diffuse. As a result, the net directional flow of Fe is balanced by an opposite flow of vacancies, which can condense into pores at dislocations. This phenomenon was first observed in the movement of the interface between a diffusion couple of copper and zinc in brass as a result of the different diffusion rates of these two species at high temperature. EDS mapping of the iron oxide microparticle is shown in Figures 1(d)-(e). Both Fe and O have a uniform distribution on the surface and inside the particle. In contrast to the pure Fe particle, the surface of the oxidized Fe particle is composed of multiple grains containing two types of nanostructures: nanowires (Figure 1(c)) and nanopores (Figure 1(f)). XRD analysis in Figure 2(b) indicates

that these structures are composed of pure Fe_2O_3, a result consistent with EDS mapping. The nanowires have a relatively uniform diameter of 100nm±30nm and form at the center of the grains, and the nanopores have diameters of 140-300nm and also form at the center of the grains. The formation of Fe_2O_3 nanowires through thermal oxidation has been previously documented.[24,25] There are also similar reports on CuO[26] and ZnO[27] nanowire growth via thermal oxidation. There are currently three types of growth mechanisms proposed in the literature. The first is a vapor-liquid-solid/vapor-solid/liquid-solid (VLS) process.[28] Here, a metal foil or particle liquefies at a temperature that is higher than its melting temperature, and the molten liquid metal becomes vapor and active for oxidation. This applies to metals with a relatively low melting temperature. The second is self-catalytic growth, in which metal plays the role of both reactant and catalyst simultaneously. Similarly to the VLS mechanism, reaction temperatures higher than metal melting temperatures are essential. The third is stress-driven mass transport,[29] which is caused by oxide grain volume expansion and does not require liquid or gas phase formation of metals. In our work, the reaction temperature is 700°C, which is much lower than the melting temperature of Fe microparticles or nanoparticles. Fe particles of 8μm and 150nm in diameter have a melting temperature of 1408°C and 1075°C, respectively.[30] Usually, the VLS growth is of a 1D crystal growth mechanism that is assisted by a metal catalyst. The catalyst ought to be clearly visible on top of the 1D crystal. In the single phase Fe microparticle system, no catalyst is used or observed on the top of Fe_2O_3 nanowires as in Figure 1 and Figure 8. Consequently, the reasoning based on the catalyst effects can not be satisfied. Further, the VLS model can only describe 1D crystal growth through direct adsorption of a gas phase onto a solid surface. Thus it can only explain the growth of nanowires but cannot explain the nanopore formation. Therefore, the first and second types of growth mechanisms as described cannot be valid. We therefore believe that the co-existence of nanowires and nanopores can be ascribed to the third mechanism.

We observe that curvature plays a significant role in determining whether individual Fe_2O_3 grains in the multiple-grain Fe_2O_3 layer grow into either wires or pores. Our speculated mechanism for the steady state growth of nanowires and nanopores via stress-driven mass transport and the influence of positive and negative grain/crystallite surface curvature is schematically outlined in Figure 3. Typical single grains with positive and negative curvatures are marked in blue and red, respectively. In both cases the stress caused by the 30% volume expansion during oxidation becomes a driving force for the nanostructure growth. When the grain/crystallite has a positive surface curvature as shown in Figure 3(a), the outward diffusion flux of Fe atoms serves as a continual source of Fe^{3+} ions for nanowire growth and continues as long as the compressive stress in the Fe_2O_3 layer is maintained by volume expansion. Nanowires will protrude perpendicularly to the grain surface due to the mechanical stress between neighboring grains. This process was observed in electrochemically-grown aluminum oxide nanopores and explained with a similar stress-driven mechanism through a self-organization process.[22] When the surface has a negative curvature as illustrated in Figure 3(b), the oxide tends to grow at the grain boundary because of the mechanical stress that is perpendicular to the surface. Since the Fe^{3+} diffusion and O^{2-} diffusion are both perpendicular to the surface, the material can only expand in the vertical direction, which pushes the pore walls upwards. Clearly, there is only one nanopore within a single grain as the equilibrium is maintained as a result of the mechanical stress.

Redox cycles were also carried out with the Fe microparticles at 700°C. An SEM image of a particle that had undergone one full redox cycle displayed no nanopore or

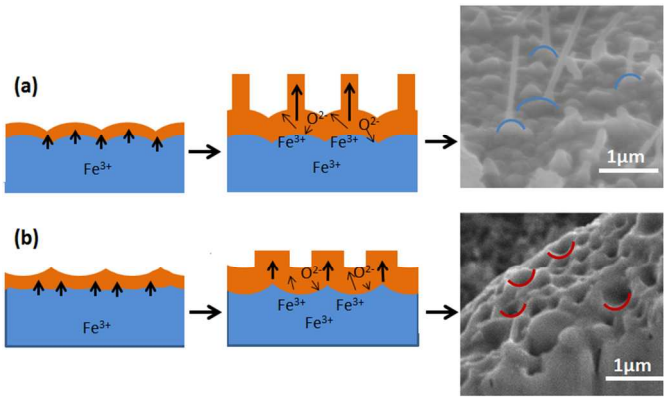

Figure 3. Growth mechanisms of (a) iron oxide nanowires and (b) iron oxide nanopores.

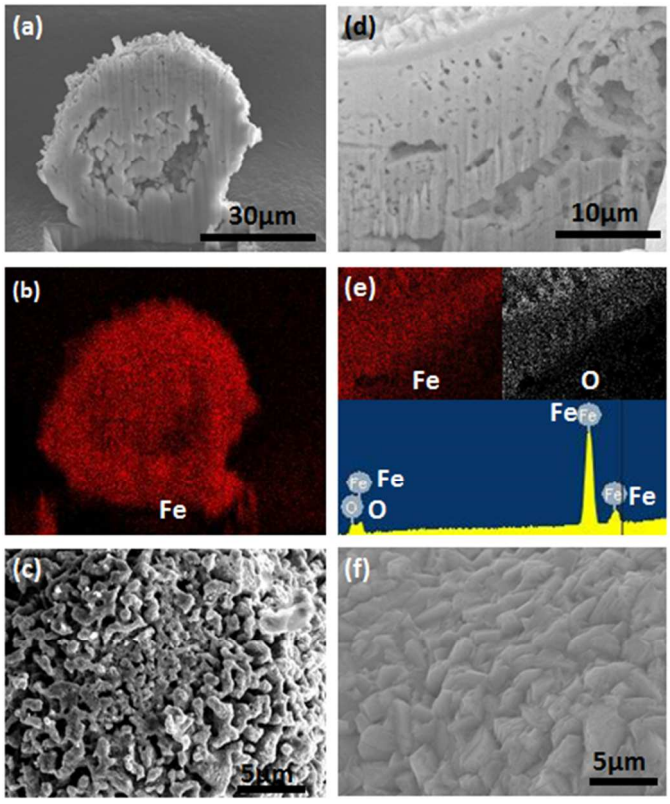

Figure 4. Characterization of Fe particle after one oxidation-reduction cycle. (a) SEM image of cross section; (b) EDS mapping; and (c) SEM image of surface; Characterization of Fe particle after five oxidation-reduction cycles. (d) SEM image of cross section; (e) EDS mapping and (f) SEM image of surface

nanowire nanostructures at its surface (Figure 4) but did possess a porous center (Figure 4(a)) and a uniform internal Fe elemental distribution (Figure 4(b)) in the particle. Very little oxygen was detected in the particle with EDS. This is in agreement with the XRD result in Figure 2(c), which reveals a particle composition of primarily Fe and trace amounts of Fe_3O_4 after one redox cycle. Many micropores with sizes of 500nm-1μm are visible on the particle surfaces (Figure 4(c)). The disappearance of the Fe_2O_3 nanowires and nanopores upon the reduction step and appearance of micropores can be explained by the outward diffusion of oxygen ions during the reduction in equation (2):

$$O_O^X = ½O_2 + V_{\ddot{O}} + 2e \quad (2)$$

This indicates the creation of oxygen vacancies $V_{\ddot{O}}$ during the reduction. The aggregation of vacancies results in pore formation which causes the disappearance of nanowires and the creation of micropores throughout the particle volume.

Although the co-existence of Fe_2O_3 nanowires and nanopores are universally observed in Fe microparticles after the oxidation in the first redox cycle, no nanowires or nanopores were observed after oxidation in the second redox cycle, as can be seen in Figure 5(a)-(b). This result further substantiates that the growth of nanowires is due to a stress-driven mass transport mechanism. That is, during the first redox cycle, we observe nanowire and nanopore growth due to a large surface stress caused by volume expansion. Many voids formed inside the microparticles during the first redox cycle (Figure 4(a)). These voids promote internal ionic transport, diffusion and volume expansion and decrease the particle surface stress during the second cycle. Consequently, under lower surface stress, no nanowires or nanopores form. If the nanowires were formed by the VLS model, we should have seen a similar nanowire growth pattern in the second redox cycle. After five redox cycles, the particle displays a porous center (Figure 4(d)) similar to that of the particle that had undergone one redox cycle. Most of the iron oxide reduces to iron except for some iron oxide near the surface (Figure 4(e)). XRD suggests that the total amount of Fe_3O_4 at the microparticle surface increases after five cycles (Figure 2(d)). While the particle surface is rough (Figure 4(f)), it is less porous as compared to the surface after one redox cycle (Figure 4(c)) due to sintering, which generally densifies particle surfaces and decreases surface areas. Sintering is unavoidable at high temperatures and becomes more severe with heating time. In this case, it is observed that sintering leads to the formation of some irreversible Fe_3O_4 agglomerates which will ultimately lead to particle deactivation when only pure Fe is used in redox applications.[31]

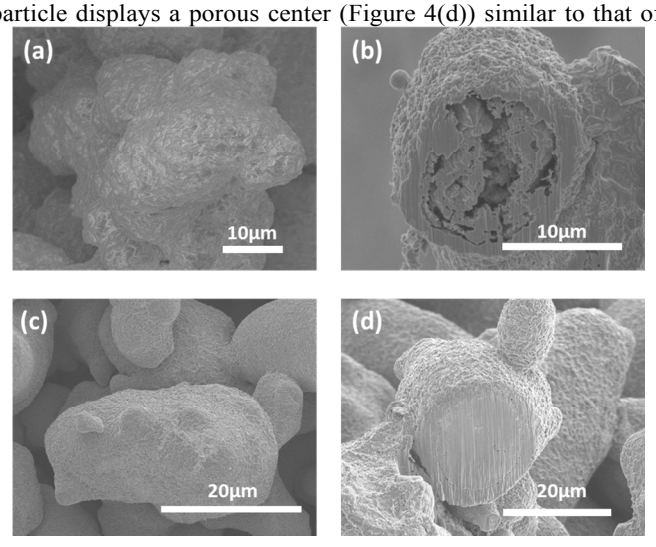

Figure 5. SEM images of oxidized Fe and FeNi microparticles in the second redox cycle. (a) Surface of a typical Fe microparticle; (b) Cross section of a typical Fe microparticle; (c) Surface of a typical FeNi microparticle; (d) Cross section of a typical FeNi microparticle.

3.2. Cyclic iron-nickel redox reactions and novel structure growth

In this section, we discuss the binary FeNi microparticle system and study the impact of nickel addition. The FeNi microparticle has a solid, non-porous surface (Figure 6(a)) and consists of the highly crystalline $Fe_{0.64}Ni_{0.36}$ phase (XRD, Figure 7(a)). A non-destructive cross section (Figure 6(b)) clearly reveals that the internal and surface morphology of the particle are both non-porous. Upon oxidation, the particle experiences a mean volume expansion of approximately 30% and the formation of a porous center, similar to the pure Fe particle. A typical SEM cross-sectional image of a single particle is shown

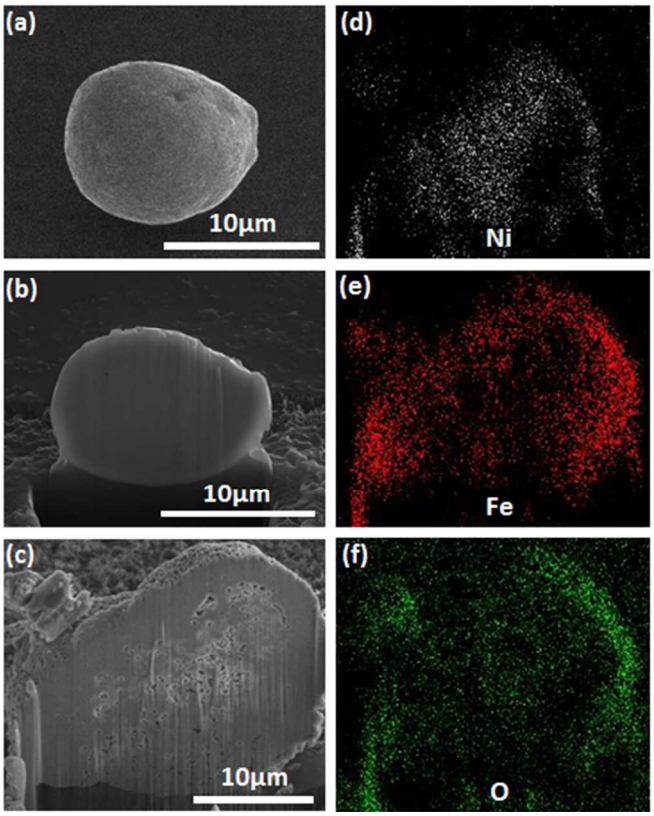

Figure 6. Characterization of FeNi particle. (a) SEM image of the surface; (b) SEM image of the cross section; (c) SEM image of the cross section after oxidation at 700°C for 0.5 hour; (d) EDS mapping of Ni from (c); (e) EDS mapping of Fe from (c); (f) EDS mapping of O from (c)

in Figure 6(c). Oxidation also results in Fe_2O_3 nanowire (Figure 8(a)) and nanopore (Figure 8(b)) growth, both of which are clearly visible on the particle surface. EDS spectra of the nanostructures suggest a pure Fe_2O_3 phase. As explained in the previous section, the growth of nanowires and nanopores correlates with the positive and negative curvature of the individual grains.

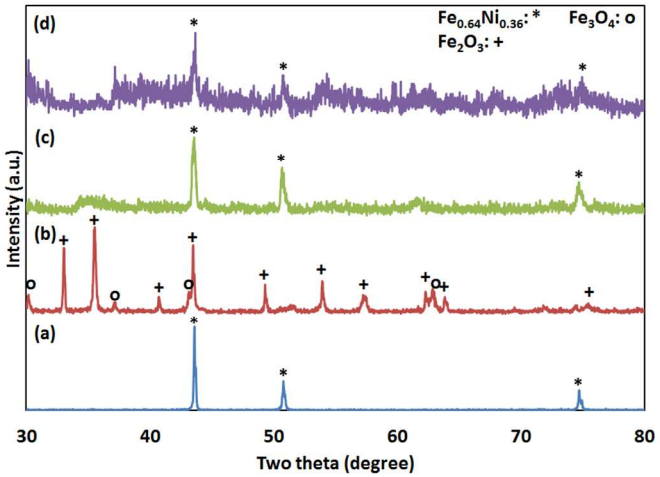

Figure 7. XRD of FeNi particle. (a) fresh (b) after oxidation (c) after one oxidation-reduction cycle (d) after five oxidation-reduction cycles

Interestingly, the EDS of the cross sections of these oxidized particles reveal an iron oxide rich shell and nickel oxide rich core structure (Figures 6(d)-(f)). Figure 7(b) confirms that the particle surface is an iron oxide shell and consists of only Fe_2O_3 and a minority of and Fe_3O_4 phases, with no NiO phase. This may be due to the XRD penetration on iron oxide that is less than the thickness of the shell layer[32]. The missing NiO phase

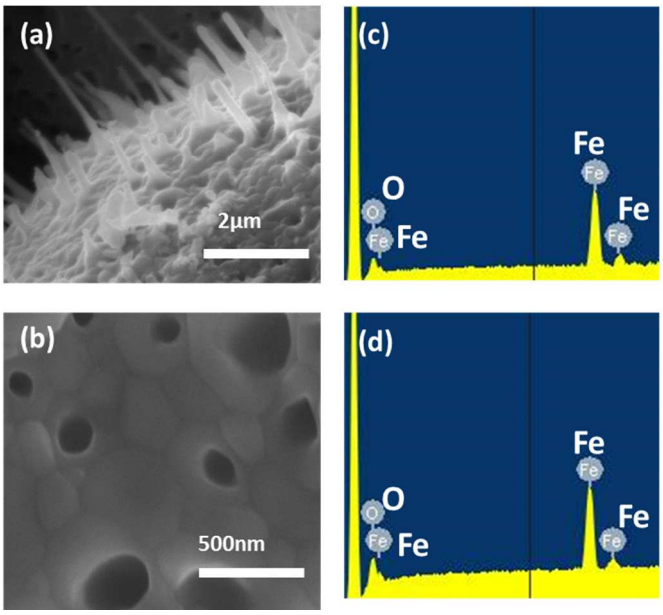

Figure 8. Characterization of FeNi particle after oxidation. (a) SEM image of Fe_2O_3 nanowires; (b) SEM image of Fe_2O_3 nanopores; (c) EDS spectrum of nanowires; (d) EDS spectrum of nanopores

can also be caused by the formation of amorphous NiO. The formation of heterogeneous core-shell structures from homogeneous FeNi microparticles can be described by a complex interplay of metal oxidation rates, ion diffusion kinetics, and mechanical expansion that is summarized as a multi-step process in Figure 9. This process is similar to the internal oxidation mechanism proposed by Wagner.[33] In the first step, oxygen contacts the particle surface, diffuses inwards, and oxidizes the nickel to yield a mixed particle with NiO and Fe. Ni will fully oxidize to NiO throughout the entire particle before Fe undergoes appreciable oxidation because Ni has a significantly faster oxidation rate ($1.6x10^{-11}cm^2/s$) than Fe ($9.7x10^{-15}cm^2/s$).[34,35,36] The oxidation can also be written as the consumption of oxygen vacancies as in equation (1). This will yield an expansion of the crystal lattice near the Ni atoms, as the calculated volume expansion of Ni to NiO is 21%. We note that NiO is a p-type semiconductor due to the non-stoichiometry of NiO, such that it contains excess Ni vacancies V_{Ni}''. The reaction rate of Ni oxidation is further enhanced by the formation of Fe^{3+}, which is an aliovalent substitution that will fill in V_{Ni}'' and create negatively charged electrons (e):

$$e + h = \text{null} \quad (3)$$

which shifts the oxidation reaction (1) to the right. Once the Ni is oxidized to NiO, it will no longer react with O_2. In the second step, the outermost layer of Fe will eventually oxidize to Fe_2O_3 under an oxygen atmosphere, due to the large concentration of oxygen ions at the surface of the particle. The majority of Fe atoms in the particle core are not oxidized yet due to the high-to-low oxygen concentration gradient from the surface to the core. In the third step, the Fe_2O_3 grains will continue to grow on the surface and merge to form a continuous layer. Here, Fe atoms from the core continuously diffuse to the surface because the consumption of Fe atoms at the surface from oxidation yields a concentration gradient of Fe atoms. As discussed in the Fe system, the outward Fe diffusion coefficient is higher than the inward oxygen diffusion coefficient in iron oxide. Additionally, the 30% volume expansion rate of Fe to Fe_2O_3 creates physical space for the Fe ions to diffuse. It is noted that Fe has different oxidation states, and the O_2- concentration gradient within the particle yields an inner layer of FeO growing underneath the Fe_2O_3 layer through reaction (5):[37]

$$Fe + 3/2O_2 = 1/2Fe_2O_3 \quad (4)$$

$$Fe + 1/2O_2 = FeO \quad (5)$$

$$FeO + Fe_2O_3 = Fe_3O_4 \quad (6)$$

In the fourth step, all of the Fe will convert to its oxide states through reactions (4)-(6), and a thick outermost layer of Fe_2O_3 and a thin Fe_3O_4 inner layer will surround a porous NiO-rich core. The voids in NiO are volumes initially occupied by the Fe that had diffused outwards to the particle surface forming the shell. This outward diffusion of Fe can again be related to the

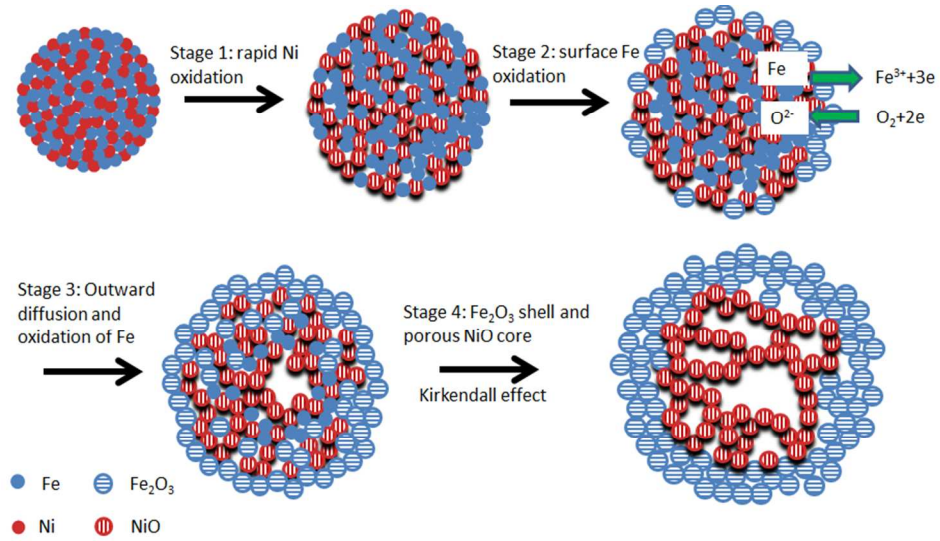

Figure 9. Core-shell structure formations in oxidized FeNi

Kirkendall Effect, similar to that observed in pure Fe microparticles in the previous section. Here, atomic diffusion occurs through vacancy exchange, as opposed to the direct interchange of atoms.

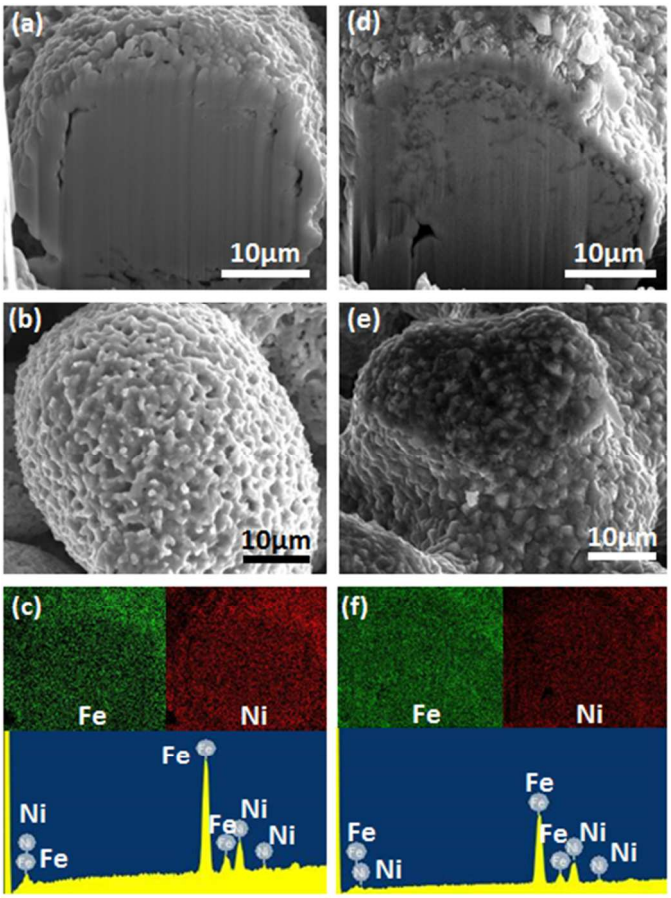

Figure 10. Characterization of FeNi particle after one oxidation-reduction cycle. (a) SEM image of cross section; (b) SEM image of surface; and (c) EDS mapping and spectrum of surface; Characterization of FeNi particle after five oxidation-reduction cycles. (d) SEM image of cross section; (e) SEM image of surface; and (f) EDS mapping and spectrum of surface

The microstructure of the active FeNi particles gradually changes over multiple redox cycles. Figure 10(a) and (d) are the cross sections of the FeNi particles after one and five cycles, respectively, and EDS analysis (Figures 10(c) and (f)) suggests a uniform distribution of both Fe and Ni. The core-shell structure disappears after oxidation-reduction cycles. Figures 10(b) and (e) show the particle surfaces after one and five cycles, respectively. The particles return to their original structure after one cycle, except for the formation of a much rougher and more porous surface and of a porous layer underneath the surface. However, after five cycles of oxidation-reduction reactions (Figure 10(e)), the particle is largely distorted from its original shape. Similar to the Fe system, no nanowires or nanopores can be observed after the second oxidation as can be seen in Figure 5(c) and (d) for the same reason explained in the previous section. Meanwhile, the sintering effect is more severe after five cycles. This is the effect that has been found in many complex metal oxide materials and causes an overall decreasing particle surface area and deterioration of reactivity.

Our study clarifies the role of Ni in Fe_2O_3 nanowire growth. Chueh *et al* studied FeNi alloy foils and argued that increasing the concentration of Ni in the alloy foil will increase the density of Fe_2O_3 nanowires. This is in conflict with the work by Wulf and co-worker.[35] In spite of the fact that the density of the nanowires fluctuates with grain sizes in a single Fe_2O_3 particle, an estimation of nanowire density can be obtained by careful comparison of Figure 1(c) and Figure 8(a). We estimate the growth of approximately 45 nanowires in Figure 1(c) and approximately 40 nanowires in Figure 8(a) within an area of about 50μm^2. This indicates that Ni composition does not increase Fe_2O_3 nanowire density in iron metal or alloy systems and that Ni has a negligible effect on the growth of the nanostructures.

3.3. Cyclic copper-nickel redox reactions

In the previous discussion of FeNi cycling, we observed that oxidation rate and volume expansion are two key factors for core-shell formation. In addition, high volume expansion and surface curvature led to the growth of nanowires and nanopores. To further analyze the role of oxidation rate and volume expansion in microparticle morphology, we analyze CuNi binary alloy systems. In this system, the oxidation rate of Cu is $3x10^{-12}cm^2/s$ and similar to the oxidation rate of Ni as mentioned in previous section.[38] Therefore, Cu and Ni will oxidize nearly simultaneously, which is unlike the case of the FeNi system. In addition, Cu^{2+} is an isovalent substitution and cannot create any electron or hole while filling a Ni vacancy, meaning that the Ni oxidation rate will not be affected by any Cu^{2+} formation. Given our prior analysis of FeNi, we therefore expect that oxidized CuNi microparticles will not yield a core-shell morphology. Experimental results indeed demonstrate a full conversion of CuNi to CuO and NiO after oxidation, and no core-shell structure is observed, as confirmed in EDS mapping of Cu, Ni and O in Figures 11 (d), (e), and (f), respectively. These three elements are uniformly distributed in the whole oxide particle, which is very different from the FeNi system. It is also observed that a porous oxide center forms, similar to the Fe and FeNi particles, as a result of the Kirkendall effect.

Clear grain boundaries with grain sizes of 0.3-2μm can be observed in Figure 11(c) in the copper nickel oxides. These

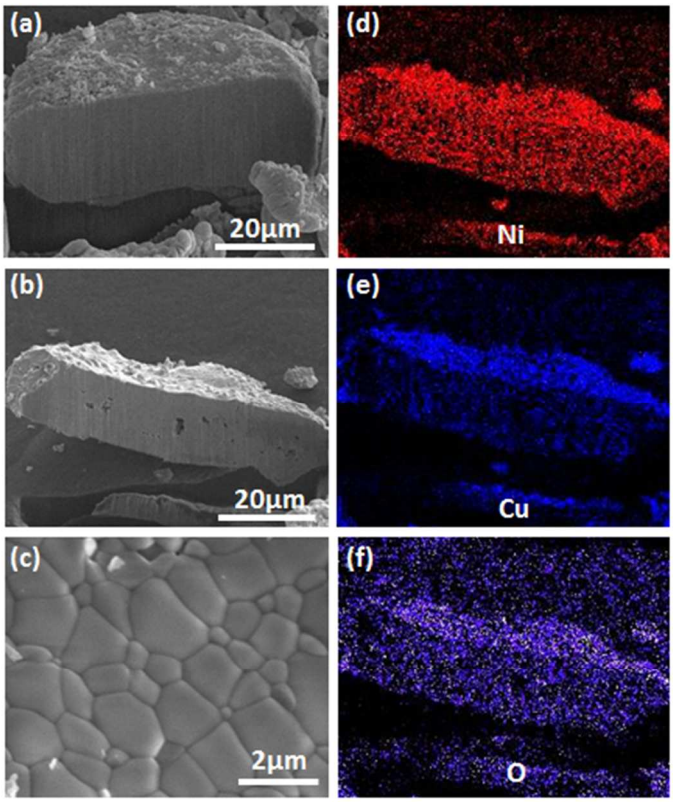

Figure 11. Characterization of CuNi particle. (a) SEM image of cross section of a CuNi particle; (b) SEM image of cross section of a particle after oxidation at 700°C for 0.5 hour (c) SEM image of the top surface of an oxidized particle; (d) EDS mapping of Ni from (b), (e) EDS mapping of Cu from (b), (f) EDS mapping of O from (b)

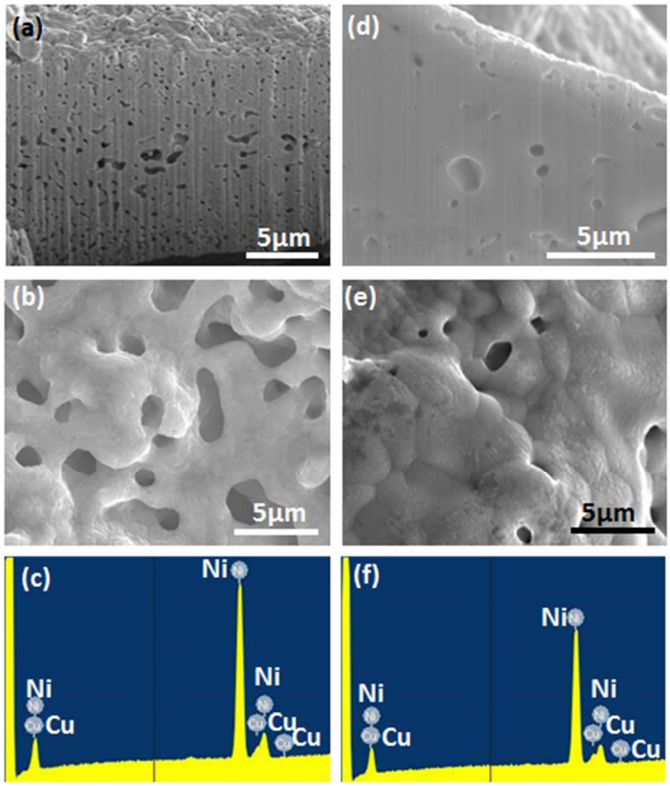

Figure 12. Characterization of CuNi particle after one oxidation-reduction cycle. (a) SEM image of cross section; (b) SEM image of surface; and (c) EDS spectrum of surface; Characterization of CuNi particle after five oxidation-reduction cycles. (d) SEM image of cross section; (e) SEM image of surface; and (f) EDS spectrum of surface

grain boundaries are defects caused by mechanical stress during ionic transport and the formation of oxide phases. However, no oxide nanowires or nanopores are observed in CuNi systems for two reasons. First, the mechanical stresses created by the oxidation of Cu (20% volume expansion of Cu to CuO) and Ni (21% volume expansion of Ni to NiO) are similar and are both lower than that of iron oxide. Hence, the driving force for nanowire growth in the CuNi system is smaller than that in the FeNi system, and the difference may result in substantial changes in nanostructure growth. A higher mechanical stress during metal oxidation can result in a much more uniform nanopore arrangement, as in the case of porous alumina (50% lower than metal aluminum atomic density). Second, we do not see large positive or negative surface curvature within individual grains in the SEM images. As discussed in a previous section, the curvature can play an important role in nanowire and nanopore growth, when the growth mechanism is dictated by stress-driven mass transport.

In a manner very similar to the Fe and FeNi systems, pores within the CuNi microparticles form after oxidation-reduction cycles, with pore sizes of 2-3μm. As shown in Figures 12(c) and (f), all the pores are interconnected with uniform elemental distribution after one and five cycles. While all of the Cu converts to metallic Cu with minimal copper oxide impurities after the oxidation-reduction cycles, such is not the case for

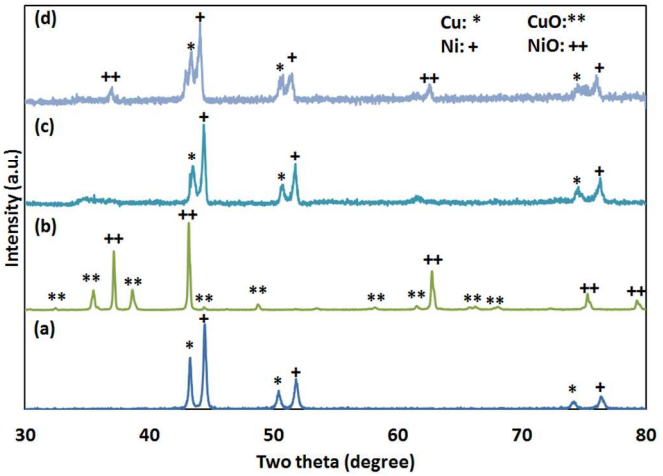

Figure 13. XRD of CuNi particle (a) fresh (b) after oxidation (c) after one oxidation- reduction cycle (d) after five oxidation-reduction cycles

NiO. Although little NiO can be detected after one redox cycle (Figure 13(c)), the amount of NiO after five oxidation-reduction cyles becomes more notable as shown in Figure 13(d). This is due to the fact that severe sintering hinders the reduction from being fully achieved under the experimental conditions.

4. Conclusion

There exists limited knowledge about the structural changes in metal oxide particles on the nanoscale during redox reactions, which are key to their performance on a macroscopic level. This study focused on the cyclic oxidation-reduction reactions of Fe, FeNi, and CuNi systems. Upon oxidation, nanopores and nanowires were observed at the surface of Fe and FeNi microparticles, and the morphology of the FeNi microparticles changed into a core-shell structure. These phenomena were ascribed to processes associated with ion transport, diffusion, and volume expansion. Upon multiple cycles, the Fe and FeNi nanowires disappear and the formation of micropores were observed throughout the Fe and FeNi microparticles due to the aggregation of vacancies. These phenomena provide a fundamental basis for understanding transformations occurring during the redox rate process for the metal oxide composite materials. A thorough understanding of the behavior of these metal oxide systems at the nanoscale level can yield better strategies for material selection and design for applications including chemical looping. This work not only explains the morphological changes during the redox reactions in FeNi, Fe and CuNi systems, but also provides an insight into the possible self-organized structural growth in many other systems. This methodology has been applied to study more complicated materials including quaternary systems such as FeNiMnCu. Our future work will include studying these growth and transformation mechanisms through DFT calculations and Monte Carlo simulations and studying similar reactions in Fe and FeNi thin film systems.

Acknowledgements

The helpful discussion with Elena Chung and the valuable instrumentation support provided by the Ohio State Electron Spectroscopy Center are gratefully acknowledged.

Notes and references

[a] Department of Chemical and Biomolecular Engineering, The Ohio State University, 140 West 19th Ave, Columbus, OH 43210, USA.
[b] Department of Electrical Engineering, Ginzton Laboratory, Spilker Engineering and Applied Sciences, 348 Via Pueblo Mall, Stanford University, Stanford, CA 94305, USA.
*To whom correspondence should be addressed; Email: fan.1@osu.edu
See DOI: 10.1039/b000000x/

1 I. A. Kuznetsov, M. J. Greenfield, Y. U. Mehta, W. Merchan-Merchan, G. Salkar and A. V. Saveliev, *Appl. Energy*, 2011, **88**, 4218-4221.
2 J. Suntivich, H. A. Gasteiger, N. Yabuuchi, H. Nakanishi, J. B. Goodenough and Y Shao-Horn, *Nat. Chem.*, 2011, **3**, 546-550.
3 M. R. Hoffmann, S. T. Martin, W. Choi, and D. W. Bahnemann, *Chemical Reviews* 1995, **95,** 69-96.
4 L.-S. Fan, *Chemical Looping Systems for Fossil Energy Conversions*, Wiley-AIChE, Hoboken, NJ, 2010.
5 H. Dotan, O. Kfir, E. Sharlin, O. Blank, M. Gross, I. Dumchin, G. Ankonina and A. Rothschild, *Nature Materials***,** 2013, **12**, 158–164**.**
6 L.-S. Fan and F. Li, *Ind. Eng. Chem. Res.*, 2010, **49**, 10200-10211.
7 D.D. Figueroa, T. Fout, S. Plasynski, H. McIlvried and R. D. Srivastava, *Int. J. Greenhouse Gas Control*, 2008, **2**, 9-20.
8 L.-S. Fan, L. Zeng, W. Wang and S. Luo, *Energy Environ. Sci.,* 2012, **5**, 67254-7280.
9 A. Lyngfelt, *Oil Gas Sci. Technol.*, 2011, **66**, 161-172.
10 L. Zeng, S. Luo, D. Sridhar and L.-S. Fan, *Rev. Chem. Eng.*, 2012, **28**, 1-42.
11 J. Adánez, L. F. de Diego, F. García-Labiano, P. Gayán and A. Abad, *Energy Fuels*, 2004, **18**, 371-377.
12 T. Mattisson, H. Leion and A. Lyngfelt, *Fuel*, 2009, **88**, 683-690.
13 F. Li, H.-R. Kim, D. Sridhar, F. Wang, L. Zeng, J. Chen and L.-S. Fan, *Energy Fuels*, 2009, **23**, 4182-4189.
14 Q. Song, R. Xiao, Z. Deng, W. Zheng, L. Shen and J. Xiao, *Energy Fuels*, 2008, **22**, 3661-3672.
15 S. Bhavsar and G. Veser, *Ind. Eng. Chem. Res.*, 2013, **52**, 15342–15352.
16 M. Rydén, M. Johansson, E. Cleverstam, A. Lyngfelt and T. Mattisson, *Fuel*, 2010, **89**, 3523-3533.
17 J. Adanez, F. Garcia-Labiano, L.F. de Diego, P. Gayan, J. Celaya and A. Abad, *Ind. Eng. Chem. Res.* 2006, **45**, 2617– 2625.
18 S. R. Son and S. D.Kim, *Ind. Eng. Chem. Res.* 2006, **45**, 2689– 2696.
19 O. Jessensky, F. Muller and U. Gosele, *Appl. Phys. Lett*., 1998, **72**, 1173-1175.
20 H. J. Fan, U. Gösele and M. Zacharias, *Small*, 2007, **3**, 1660-1671.
21 R. Nakamura, D. Tokozakura, H. Nakajima, J.-G. Lee and H. Mori, *J. Appl. Phys*., 2007, **101**, 074303.
22 W. K. Chen and N. L. Peterson, *J. Phys. Chem. Solids*, 1975, **36**, 1097-1103.
23 B. Amami, M. Addou, F. Millot, A. Sabioni, and C. Monty, Ionics, 1999, **5**, 358-370.
24 Y. Fu, J. Chen and H. Zhang, *Chem. Phys. Lett.*, 2001, **350**, 491-494.
25 X. Wen , S. Wang , Y. Ding , Z. L. Wang and S. Yang, *J. Phys. Chem. B*, 2005, **109**, 215-220.
26 M. Farbod, N. M. Ghaffari and I. Kazeminezhad, *Ceram. Int.*, 2014, **40**, 517-521.
27 H. Y. Dang, J. Wang and S. S. Fan, *Nanotechnology*, 2003, **14**, 738–741.

28 T.-W. Kim, T. Kawazoe, S. Yamazaki, M. Ohtsu and T. Sekiguchi, *Appl. Phys. Lett.*, 2004, **84**, 3358– 3360.
29 C. X. Zhao, Y. F. Li, J. Zhou, L. Y. Li, S. Z. Deng, N. S. Xu and J. Chen, *Cryst. Growth Des.*, 2013, **13**, 2897–2905.
30 Q. Shu, Y. Yang, Y.-T. Zhai, D. Y. Sun, H. J. Xiang and X. G. Gonga, *Nanoscale*, 2012, **4**, 6307-6311.
31 F. Li, Z. Sun, S. Luo and L.-S. Fan, *Energy Environ. Sci.*, 2011, **4**, 876-880.
32 M. E. Fitzpatrick, A. T. Fry, P. Holdway, F. A. Kandil, J. Shackleton and L. Suominen, *Measurement Good Practice Guide No. 52*, 2005.
33 C. Wagner, *Zeitschrift fur Elektrochemie*, 1959, **63**, 772-782.
34 A. M. Huntz, B. Lefevre and F. Cassino, *Mater. Sci. Eng.,* A, 2000, **290**, 190–197.
35 G. L. Wulf, T. J. Carter and G. R. Wallwork, *Corros. Sci.*, 1969, **9**, 689–690.
36 F. García-Labiano, J. Adánez, L. F. de Diego, P. Gayán and A. Abad, *Energy Fuels,* 2006, **20**, 26-33.
37 L. Yuan, Y. Wang, R. Cai, Q. Jiang, J. Wang, B. Lid, A. Sharmae and G. Zhou, *Mater. Sci. Eng.,* B, 2012, **177**, 327–336.
38 Y. Zhu, K. Mimura and M. Isshiki, *Mater. Trans., JIM*, 2002, **43**, 2173-2176.